NASA TECHNICAL NOTE

NASA TN D-5454

NASA TN D-5454

CASE FILE COPY

FLOW-FIELD AND DRAG CHARACTERISTICS OF SEVERAL BOUNDARY-LAYER TRIPPING ELEMENTS IN HYPERSONIC FLOW

by Allen H. Whitehead, Jr.

Langley Research Center
Langley Station, Hampton, Va.

NATIONAL AERONAUTICS AND SPACE ADMINISTRATION • WASHINGTON, D. C. • OCTOBER 1969

1. Report No. NASA TN D-5454	2. Government Accession No.	3. Recipient's Catalog No.
4. Title and Subtitle FLOW-FIELD AND DRAG CHARACTERISTICS OF SEVERAL BOUNDARY-LAYER TRIPPING ELEMENTS IN HYPERSONIC FLOW		5. Report Date October 1969 6. Performing Organization Code
7. Author(s) Allen H. Whitehead, Jr.		8. Performing Organization Report No. L-6452 10. Work Unit No. 126-13-10-21-23
9. Performing Organization Name and Address NASA Langley Research Center Hampton, Va. 23365		11. Contract or Grant No. 13. Type of Report and Period Covered Technical Note
12. Sponsoring Agency Name and Address National Aeronautics and Space Administration Washington, D.C. 20546		14. Sponsoring Agency Code
15. Supplementary Notes		

16. Abstract

Flow-field and drag characteristics of several tripping-element shapes have been examined under laminar-boundary-layer conditions at a free-stream Mach number of 6.8 to assess the contribution of the elements to the drag of wind-tunnel models and to examine flow-field characteristics around individual element shapes. The element drag coefficient based on local conditions depends primarily on element shape, the spacing between the elements, and the ratio of the element height to boundary-layer height. Advantageously, certain element shapes have drag coefficients which are relatively independent of the ratio of element height to boundary-layer height for values of this ratio that have practical application for hypersonic wind-tunnel facilities.

17. Key Words Suggested by Author(s) Tripping elements Protuberance flow field		18. Distribution Statement Unclassified – Unlimited	
19. Security Classif. (of this report) Unclassified	20. Security Classif. (of this page) Unclassified	21. No. of Pages 38	22. Price* $3.00

*For sale by the Clearinghouse for Federal Scientific and Technical Information
Springfield, Virginia 22151

FLOW-FIELD AND DRAG CHARACTERISTICS OF SEVERAL BOUNDARY-LAYER TRIPPING ELEMENTS IN HYPERSONIC FLOW

By Allen H. Whitehead, Jr.
Langley Research Center

SUMMARY

Flow-field and drag characteristics of several tripping-element shapes have been examined at a free-stream Mach number of 6.8 to assess the contribution of the elements to the drag of wind-tunnel models and to examine flow-field characteristics around individual element shapes. The results of these flow-field studies are also applicable to the more general problem of determining the flow around protuberances extending into a hypersonic flow. The tests were performed in the Langley 11-inch hypersonic tunnel at free-stream unit Reynolds numbers per meter of 0.2×10^7 to 1.5×10^7 under known laminar-boundary-layer conditions.

The element drag coefficient based on local conditions depends primarily on element shape, the spacing between the elements, and the ratio of the element height to boundary-layer height. Advantageously, certain element shapes have drag coefficients which are relatively independent of the ratio of element height to boundary-layer height for the values of this ratio that have practical application for hypersonic wind-tunnel facilities. Oil-flow patterns indicate the interaction between neighboring elements and permit a modeling of the flow field around the protuberances.

INTRODUCTION

A serious problem in the use of tripping elements for force tests in wind tunnels is that the element drag adds an extraneous component to the vehicle drag. Several methods are available for predicting tripping-element drag at subsonic and supersonic speeds which are not universally applicable at hypersonic speeds. (See ref. 1.) A more accurate determination of the element drag is needed at hypersonic speeds because of the larger drag associated with the increased element size required for effective tripping. In reference 2, it was shown that at hypersonic speeds the element height must be on the order of the boundary-layer height to significantly affect the position of transition. Several approaches to the problem of the element drag at hypersonic speeds are considered, and a method is outlined by which the element drag contribution to the total drag of a

wind-tunnel configuration can be estimated. Accurate determination of element drag is more critical for hypersonic than for supersonic wind-tunnel conditions because the element drag addition to the model drag at lower speeds is generally less than 15 percent of the total drag, whereas at hypersonic speeds the element drag can be expected to be greater than 25 percent (ref. 3).

The flow-field studies were conducted to promote an understanding of the mechanism by which tripping elements induce transition and to obtain results applicable to the study of flow around small protruding objects.

Tests were conducted in the Langley 11-inch hypersonic wind tunnel at a free-stream Mach number of 6.8. Tripping elements were placed in a laminar boundary layer near the trailing edge of a wedge model, and the drag of these elements was determined from force-balance measurements of the wedge drag with and without the elements. Several different element sizes and shapes were tested to determine the optimum tripping element from drag consideration.

SYMBOLS

A_c	area of circle with diameter equal to element height
A_F	frontal area of single tripping element
a	width of inner vortex row at element location (see fig. 5(c))
b	width of outer vortex row at element location (see fig. 5(c))
$C_{D,M}$	drag coefficient of model with tripping elements, $C_{D,m} + C_{D,T}$
$C_{D,m}$	drag coefficient of model without tripping elements, $\frac{D_m}{q_\infty S}$
$C_{D,T}$	drag coefficient of sum of all tripping elements, $N \times \frac{q_l}{q_\infty} \times \frac{A_c}{S} \times C_{D,t}$
$C_{D,t}$	drag coefficient of single tripping element, $\frac{D_t}{q_l A_c}$
D_m	drag of wind-tunnel model without tripping elements
D_t	drag of single tripping element

k	element height
M	Mach number
N	number of tripping elements present on model
p	static pressure
q	dynamic pressure
R	unit Reynolds number
$R_{l,k}$	local Reynolds number based on k, $\frac{u_l k}{\nu}$
R_{l,x_k}	local Reynolds number based on x_k, $\frac{u_l x_k}{\nu}$
$R_{\infty,L}$	free-stream Reynolds number based on model length
S	reference area of configuration model
s	spacing between elements, center to center
T_w	wall temperature
u	velocity
w	maximum width of single element (see fig. 1(c))
x	chordwise coordinate
x_k	chordwise distance from leading edge of model to element location
y	distance above model surface
α	angle of attack
Δ	separation distance, measured from center of element to separation boundary (see fig. 12(a))

$\overline{\Delta}$ separation distance normalized with respect to total frontal area of elements, $\frac{\Delta}{NA_F}$

δ boundary-layer height at element location with elements absent

θ_{ep} half-angle of end plate

θ_m half-angle of wedge model

ν kinematic viscosity

Subscripts:

l local conditions at edge of boundary layer

∞ free stream

MODELS

The dimensions of the models and tripping elements used in this investigation are shown in figure 1. Tripping elements were mounted on both surfaces of two wedge-shaped models (fig. 1(a)). One wedge model had a half-angle of 12.6° which resulted in a local Mach number of 4.7 at the element location; the other had a half-angle of 7.7° and a local Mach number of 5.5. The thickness at the base of these models insured that the models would be properly secured to the sting. End plates eliminated the outflow at the edge of the model and thus provided an essentially two-dimensional flow field in the area of the tripping elements. The wedge models were always at a zero angle of attack.

The various tripping elements were located by templates and then tack-welded to the model surface along a spanwise line 0.50 cm from the base of the model. The photograph of figure 1(b) shows one of the wedge models with one end plate removed and five spherical tripping elements in place. Because the elements were attached to a surface inclined either 7.7° or 12.6° to the axis of the balance, the balance measured only a component of the total drag. The measured drag was estimated to be only 1 and 2 percent less, respectively, than the total drag, and this difference was neglected.

Seven different element shapes used in the investigation (sphere, cylinder, pinhead, triangular prism, rod, and two vortex-generator shapes) are shown in figure 1(c). The vortex generators were set at 45° to the flow and each shape was tested in pairs, one element angled to the left and the other to the right. Element size varied as indicated in figure 1(c) for the sphere, triangular prism, and cylinder. In general, the elements maintained a common height (k) and a common width (w).

A summary of the geometric and free-stream variables considered in this study is shown in table I. The calculated values of local Reynolds number based on element height $R_{l,k}$ and on element location R_{l,x_k} are shown for the respective free-stream Reynolds number and local Mach number. These Reynolds numbers are given here because of their usefulness in transition analysis; the appropriate $R_{l,k}$ or R_{l,x_k} value can be determined from this table and the k/δ values given in the figures.

APPARATUS AND TESTS

The investigation was conducted in the Langley 11-inch hypersonic tunnel described in reference 4. The facility is a blowdown tunnel with test durations of about 1 minute. A nominal Mach number of 6.8 in air is produced by a contoured two-dimensional nozzle constructed from invar to minimize contraction and expansion of the throat due to heat absorption. The Mach number variation during the test run is only about 1 percent after the first 10 seconds. A calibration of this nozzle can be found in reference 5. Stagnation pressures were varied from 5 to 40 atmospheres (0.5 to 4 MN/m^2) and the stagnation temperature was around 620° K; the free-stream Reynolds number per meter thus varied from 0.2×10^7 to about 1.5×10^7. The water-vapor content of the air was maintained sufficiently low to eliminate water condensation effects.

Drag measurements of the models were obtained by an external three-component strain-gage balance that was water-cooled to minimize the effects of heating. The axial-force data were adjusted to a zero-base-pressure condition. Two base-pressure measurements were obtained: one reading was obtained of the pressure inside the sting shield, and the second provided a pressure value external to the shield. (See fig. 1(a).) The values were then averaged and the resulting value applied to the entire base.

The oil-flow technique indicated the separation boundaries and revealed the surface-flow characteristics in the vicinity of the tripping elements. Prior to each oil-flow test, a mixture of silicone fluid and lampblack was distributed over the model surface in random dots of various sizes. A single-head probe was used to traverse the boundary layer. The probe head was oval-shaped and was about 0.2 cm wide and 0.015 cm high with an opening height of about 0.006 cm.

The accuracy of the element drag data depends on the ratio of element height to boundary-layer height k/δ and the number of elements present on the wedge model, which determines the value of s/w. This dependence exists because the element drag is determined by the difference between the drag of the model with and without the elements present. Since for the smaller values of k/δ and/or larger values of s/w, the magnitude of this difference can be small compared with the magnitude of the measured drag of the model, the accuracy of the element drag data under these conditions will be reduced. The

range of the possible errors resulting from balance accuracy in the values of the element drag coefficient varies from 26 percent at $s/w = 8$ and $k/\delta = 1$ to 0.3 percent at $s/w = 2$ and $k/\delta = 3$. As part of this error determination, the ratio of the element drag to the measured drag of the wedge model without elements for the conditions cited above was found to be 0.2 and 1.3, respectively. At the most common condition for which data were obtained in this study, $k/\delta = 2$ and $s/w = 4$, the error in $C_{D,t}$ was estimated at 0.8 percent. Several runs were repeated and the data were found to agree well within the calculated accuracy limits. Base-pressure measurements resulted in adjustments to the measured axial-force data of about 10 percent, and little effect was noted on those values when the elements were removed from the wedge models. Base-pressure inaccuracies are further minimized in the determination of $C_{D,t}$ since these adjustments are essentially canceled during the process of subtracting the model drag without the elements present from the drag value with the elements on the model.

APPLICABILITY OF TECHNIQUES FOR ELEMENT DRAG DETERMINATION AT SUPERSONIC SPEEDS

Two methods for obtaining the drag of tripping elements up to Mach 3 are presented in reference 1. In the first method, the drag data are plotted against unit Reynolds numbers. An extrapolated curve is then faired through the high Reynolds number data, where natural transition produces essentially all turbulent flow; the curve is extended to a lower unit Reynolds number range, where transition must be trip-induced, by following along the theoretical turbulent curve for a smooth flat plate. The element drag is then determined as the difference between this extrapolated curve and the turbulent drag data obtained with tripping elements. Because the transition Reynolds number has been shown to increase sharply beyond about Mach 3.5 (ref. 6) and because of the limitations of hypersonic ground facilities, this method is not presently applicable to hypersonic wind-tunnel testing.

In the second method of element drag determination discussed in reference 1, drag data are obtained on a model for which the element size has been varied over a moderate range. Each particle size must be sufficiently large to produce transition at or near the tripping element and yet sufficiently small not to cause undue distortions to the flow downstream of the element. A plot of the drag coefficient as a function of a tripping parameter is then constructed, and the drag data are linearly extrapolated to zero-element-size conditions. The drag increment due to any element size can be obtained from this curve. A possible fault in this method examined in reference 1 is that the data appearing in the plot described above are not necessarily linear; data are shown which indicate a sharp decrease in the model drag for the smallest element size tested. A fairing through these data will give a considerably different value of the element drag contribution than that

obtained from a fairing through the drag data produced by a model with large tripping elements. At hypersonic speeds, this problem is compounded because the critical element height below which transition will move rearward is considerably greater than at supersonic conditions. An extrapolation from this minimum element height to a zero-height condition is thus a more questionable procedure at hypersonic speeds.

RESULTS AND DISCUSSION

Experimental Boundary-Layer Height

Since the ratio of the element height to boundary-layer height (k/δ) exerts such a dominant influence over transition movement (ref. 2) and element drag (present paper), the laminar boundary layer at the element location was surveyed for the model with $\theta_m = 7.7^{\circ}$. Pitot surveys were obtained for three different Reynolds numbers. By assuming that static pressure is constant throughout the boundary layer, the total pressure profiles were converted to velocity profiles through a modified Crocco relation (ref. 7). The results are shown in figure 2(a), where the velocity ratio is presented as a function of the distance from the model wall. The value of δ is determined at the location where $u/u_l = 1$ and is indicated in this figure.

To assure that these profiles have the characteristics of a laminar boundary layer, the velocity ratio has been presented in a similarity form in figure 2(b). For similarity to be preserved, $u/u_l = f(y/\delta)$, where the functional relation must be the same at any given x value regardless of the boundary-layer thickness. The near linearity of this profile indicates the presence of a laminar boundary layer.

Monaghan's T' theory (ref. 7) was used to estimate the thickness of the boundary layer at the element location where $y = \delta$ at $u/u_l = 1$. The theoretical values are shown in figure 3 as a function of unit Reynolds number. The method of obtaining the δ values used herein is illustrated in this figure. Curves based on Monaghan's theory are shown for both adiabatic and cool-wall $\left(T_w = 310^{\circ}\ K\right)$ conditions. The wall temperature of the model was then estimated based on the length of time from the start of a run that a drag measurement was obtained. An appropriate curve was interpolated between the adiabatic and cool-wall conditions to obtain the δ values used herein. Experimental values of δ were obtained for three Reynolds numbers to check the accuracy and applicability of Monaghan's theory for the model with $\theta_m = 7.7^{\circ}$. The initial growth of the boundary layer as the model surface temperature increased was such that an accurate determination of the boundary-layer edge at $u/u_l = 1$ was difficult. The three experimental values shown in figure 3 were obtained during the latter part of a 90-second test, in which the model surface temperature was higher than the wall temperature existing when the drag measurements were obtained (within 15 seconds of the initiation of the run). The

experimental data in figure 3 thus fall above the solid line, which indicates the values calculated for a lower wall temperature.

Flow Field Around Tripping Elements

An understanding of the flow around and downstream of a tripping element is desirable in both determining the mechanism by which these elements promote transition and in assessing the drag of these elements. The oil-flow and schlieren results contribute to the general knowledge of the flow field about protuberances extending into a hypersonic flow. The oil-flow photographs of figure 4 suggest that a basic similarity exists in the flow-field characteristics around individual elements for the sphere, cylinder, triangular prism, and pinhead. The sketch shown in figure 4(a) for the sphere is typical of the flow field around these elements and shows several counterrotating vortex filaments which initiate ahead of the element and are forced around downstream of the element, scouring the surface as they go. The production of multiple vortices in the presence of a cylindrical protuberance was also noted in reference 8 where the flow patterns were obtained under turbulent-boundary-layer conditions and at supersonic speeds.

If the elements are placed close to one another, the flow field of a single element can be strongly influenced by adjacent elements. The result of this influence on the oil-flow pattern can be seen for the spherical elements in figure 5 when the spacing parameter s/w is 4 or less. As the vortex filaments are swept around the element, the resulting surface-flow patterns are compressed by the filaments of the adjacent element. As far as the transition process is concerned, several investigations have shown that the spacing of the elements has only a small influence on the transition location behind the elements provided the elements are not too close together. (See refs. 9 and 10.) For $s/w < 3$, the results of reference 9 show a rearward movement of transition; the vortex interaction when the elements are too close apparently diminishes the effectiveness of the elements as tripping devices.

Measurements of the location of these vortex boundaries from the oil-flow results indicate the influence of element spacing on the vortex filaments. The data in figure 5(c) show that the spacing between the elements has a smaller effect on the width of the inner vortex row (a) than on that of the outer vortex row (b). The boundary of the outer vortex row shows a gradual compression towards the element and the inner vortex row. Somewhere in the vicinity of $s/w = 2$, the surface-flow pattern no longer indicates the presence of this outer vortex row, and it is conjectured that one or more of the vortex filaments have been displaced upward away from the surface. Whether this behavior has any direct consequence on the pressure drag is not known at this time.

The oil-flow results of figures 5(a) and 5(b) indicate that two modes of separation are possible. Characteristic of one mode for $k/\delta = 2$ are the oil-flow patterns for

$s/w = 2, 3, 4$, and 6 in which the separation boundary forms as an approximately straight line ahead of the elements. This mode can be called two-dimensional separation. The second mode can be seen in figure 5(b) at $s/w = 8$ and 16 in which the separated region wraps itself around the element, characteristic of a three-dimensional separation. In the second mode, part of the flow is diverted between the elements, whereas the oil flow indicated that in two-dimensional separation most of the flow probably passes above the elements. Measurement and correlation of these separation distances have been made and a discussion will follow concerning a possible relation between these measurements and the corresponding element drag. Element shape also determines the type of separation boundary, as shown in figure 4. At $s/w = 8$, only the sphere produces a three-dimensional separation; the separation boundary ahead of the other three element shapes is two-dimensional.

Based on the oil-flow results of figure 4, the schlieren photograph shown in figure 6(a), and a flow model for a cylindrical protuberance (ref. 11), a simplified flow model for the spherical element is postulated in figure 6(b) to show the location and direction of the vortices ahead of the element. The oil-flow and schlieren photographs indicate that the flow separates well ahead of the elements. The shock from the separation "wedge" interacts with a bow shock wave produced ahead of the protuberance. The bow shock perhaps plays a part in the creation of the vortex filaments. The distinguishing traces ahead of the spherical element suggest that three vortex filaments are present near the surface ahead of the sphere, and physical reasoning suggests the existence of a fourth vortex. (See fig. 6(b).) As the flow passes around the element, another vortex filament apparently initiates about 90° from the stagnation point of the sphere. (See fig. 4(a).) In some instances the oil-flow trace of the upstream vortex filament disappeared; when this occurs, one or more of the filaments is assumed to be displaced upward away from the surface.

Several investigators have suggested that when transition is induced by tripping elements, the transitioning process is initiated by the interaction of these vortices. (See, for example, refs. 9 and 10.) Flow-visualization results from two recent studies (refs. 12 and 13), presented in figure 7, indicate the downstream influence of the vortices. The photographs reproduced here are considerably enlarged to show details of the flow in the vicinity of the element. Close observation of the originals of these photographs indicate a flow pattern in the vicinity of the spherical elements similar to that identified in figure 4(b); the characteristic double oil-flow trace is in evidence. The influence of these vortices on the surface-flow characteristics persists some distance downstream of the element. In figure 7(a), the location of the beginning of the turbulent boundary layer on the flat plate indicates that the traces of those vortices near the surface persist well into the turbulent boundary-layer region. The results shown for the cone (fig. 7(b)) were obtained with the fusible temperature indicator technique (ref. 14). The dark traces

produced by the vortices are indicative of a high-shear, high-temperature area and indicate a spanwise nonuniformity in the heating due to the vortices.

Element Drag Prediction

At supersonic speeds, if the lateral spacing between elements is greater than about four times the element width ($s/w > 4$), then the position of initial contamination, and hence transition, is independent of the element spacing. (See ref. 10.) A similar result was obtained in reference 9 for hypersonic speeds where an independence of transition location for $s/w > 3$ was found. The bulk of the element drag data in the present investigation were thus obtained at a lateral spacing equal to four times the element width.

Drag of spheres.- A correlation of the spherical-element drag data is presented in figure 8 where $C_{D,t}$ is plotted against k/δ. The data in this figure are taken from the models with $s/w = 4$ between the elements. The value of $C_{D,t}$, the drag coefficient for a single roughness element, is obtained by first subtracting the measured drag value of the model with no roughness from that value obtained when elements are present on the model. This result is then divided by the number of elements present on the model to obtain $C_{D,t}$. The data are obtained for two different size elements (0.238- and 0.198-cm-diameter spheres) and for two different local conditions determined by the opening angle of the wedge model. The drag coefficient $C_{D,t}$ based on local dynamic pressure exterior to the boundary layer and on the frontal area of the element $\left(A_c = A_F \text{ for a sphere}\right)$ correlates with k/δ in figure 8. The convergence to a single curve is not as complete as desirable, but the results do suggest that k/δ is the most influential parameter when the drag is reduced on this basis. An equation which will represent the mean value of the data in this correlation is given by

$$C_{D,t} = -0.23 + 0.52\left(\frac{k}{\delta}\right) - 0.051\left(\frac{k}{\delta}\right)^2 \qquad \left(1 \leqq \frac{k}{\delta} \leqq 4\right) \tag{1}$$

This correlation is based on an element spacing of $s/w = 4$. The question arises as to the effect on the relationship derived in equation (1) if the spacing were to depart from $s/w = 4$. The extent to which the drag of a single element would be affected by the proximity of its adjacent elements would be expected to depend on the spacing between elements. The oil-flow results of figure 5 indicate the strong dependence on spacing of the vortex couplet patterns around the elements for $s/w < 8$; a similar dependence of $C_{D,t}$ on s/w could be anticipated. That such a dependence does exist is indicated by the results of figure 9(a), where the drag coefficient $C_{D,t}$ divided by the value of $C_{D,t}$ at $s/w = 4$ is plotted against s/w. An s/w increase from 2 to 4 results in an increase in $C_{D,t}$ of about 40 percent. What is surprising about the results presented in this figure is that the drag per element is apparently still being influenced by the presence of its adjacent elements even for values of s/w beyond 20. In this figure the spherical-element drag is presented for $k/\delta = 2$ and 3; drag data are also included for

triangular-prism and cylindrical elements. These data points collapse to a narrow band when the value of $C_{D,t}$ at $s/w = 4$ is used to normalize the element drag at other s/w values. This correlation can only be expected to have merit for moderate values of k/δ ($k/\delta < 4$). In order that the results of figure 9 may not be misconstrued, it should be noted that although the drag per element increases with increasing s/w, the total drag decreases. An example illustrating this fact is shown in figure 9(b) in which 17 spherical elements are assumed present on a model at a spacing of $s/w = 2$. The value of the total drag $\left(N \times C_{D,t}\right)$ decreases as s/w increases and as the number of elements decreases.

To account for this s/w dependence in the correlation developed previously the following addition to equation (1) is submitted:

$$C_{D,t} = \left[-0.23 + 0.52\left(\frac{k}{\delta}\right) - 0.051\left(\frac{k}{\delta}\right)^2\right]\frac{C_{D,t}}{\left(C_{D,t}\right)_{\frac{s}{w}=4}} \tag{2}$$

Drag of other element shapes.- Because there is considerable interest in the use of tripping-element shapes other than spheres for tripping the hypersonic boundary layer, the drag characteristics of triangular prisms, cylinders, pinheads, and two vortex-generator shapes were tested. Sketches and dimensions of these elements are given in figure 1(c). The vortex generators were set at 45° to the flow and each shape was tested in pairs, one element angled to the left and the other to the right. In reference 3 a study of the tripping effectiveness of a variety of element shapes (cylinders, spheres, triangular prisms, pyramids, and pinheads) was made, and it was found that the shape of the tripping element is not too important in producing transition at hypersonic speeds as long as an appreciable part of the frontal area of the element is located near the top of the element. A similar result was reported in reference 13, where a limited study of the effects of element shaping on transition indicated that cylinders and spheres had about equal tripping effectiveness. On this basis the pinhead tripping element was thought to show promise. It was shown to have a tripping effectiveness comparable with or slightly better than that of the other elements (ref. 3); yet its reduced frontal area should result in a reduced pressure drag.

The results of these tests are shown in figure 10 for a k/δ range of 1 to 3. The triangular prism and cylindrical elements exhibit the same general trend with k/δ; that is, at $k/\delta < 2$, the drag coefficient shows a rapid initial increase and as k/δ increases further, $C_{D,t}$ levels off. The k/δ value at which the $C_{D,t}$ value levels off and the magnitude of this asymptotic value of $C_{D,t}$ is strongly influenced by the element shape.

The major difference between the drag characteristics of the spheres as compared with the other elements shown in figure 10 is that over the range of $k/\delta = 2$ to 3, which is the range most often used for tripping hypersonic boundary layers, all element shapes exhibit relatively constant drag values (< 13-percent change) except the sphere which

shows a 50-percent increase in $C_{D,t}$ for this k/δ range. The curve based on equation (1) for the spherical elements is repeated in figure 10 to facilitate the comparison of the drag coefficient for the spherical element with those of the other element shapes. The triangular-prism and cylindrical elements exhibit the smallest changes in $C_{D,t}$ above $k/\delta = 2$. A cylinder with a height equal to twice its diameter ($k/w = 2$) was tested, and its drag coefficients are plotted in figure 10(b) to show that the k/δ independence, once established, probably holds true for higher values of k/δ as long as the same element spacing is maintained. For the triangular prism and cylindrical elements, then, the drag coefficient above $k/\delta = 2$ can be predicted to a reasonable accuracy with a rather imprecise estimate of δ. Because the value of δ is often difficult to obtain experimentally or predict analytically on complex wind-tunnel models, these two element shapes appear to offer a real advantage over the commonly employed spherical tripping elements.

The desirability of the other element shapes is questionable. The pinhead produces a drag value comparable with the other element shapes and is thus neither markedly superior in tripping effectiveness or in its drag characteristics; a disadvantage of this element is the difficulties encountered in machining and mounting the pinhead. The fin generator exhibits a comparatively low drag coefficient which shows only a small variation with k/δ. This advantage is not further pursued, however, because the tripping effectiveness of this vortex generator at hypersonic speeds has not been determined.

The values of the drag coefficients for all element shapes should tend toward their respective inviscid values as both k/δ and s/w increase. However, as long as the spacing is such that one element influences the flow around its adjacent elements ($s/w < 8$ in these experiments), then the values of $C_{D,t}$ do not increase asymptotically toward an inviscid value but can be expected to level off at a somewhat lower value. A comparison of the data of figure 10 and the corresponding Newtonian $C_{D,t}$ values shows $C_{D,t}$ values well below the theoretical inviscid level. The extent of the deviation from inviscid theory varies considerably among the different element shapes. Newtonian theory suggests a much larger variation in the magnitude of the drag coefficient due to element shape than is observed. Separation ahead of the element probably plays a role in reducing the influence of shape on the drag of the elements.

Practical consideration of tripping elements.- To provide an assessment of the magnitude of the element drag on a typical wind-tunnel configuration that would be predicted by the results of this study, figure 11 was constructed. Data for such a configuration were obtained from the results reported in reference 15, where the model was tested without tripping elements present. The configuration is a highly swept delta wing attached to a half-cone body and is shown schematically in figure 11. Calculations of the total element-drag coefficient are made for the spherical and cylindrical elements. (Details of the calculations are given in the appendix.) The $C_{D,T}$ value is normalized by the

value of the total configuration drag coefficient $C_{D,M}$, which is obtained by adding a previously measured drag coefficient for the selected model without tripping elements $C_{D,m}$ (ref. 15) to the calculated element drag coefficient $C_{D,T}$. The data from reference 15 were obtained in the same facility in which the present study was conducted $\left(M_\infty = 6.8;\ R_{\infty,L} = 1.4 \times 10^6\right)$. In the example illustrated by figure 11, the angle of attack of the wing-body combination is assumed to vary from -3° to 5° and k/δ is assumed equal to 2 at an angle of attack of 0°. By assuming that the elements lie on a flat surface, the element drag coefficient is determined for the lower and upper surfaces at the k/δ value determined by the angle of attack of the local surface.

The variation in $C_{D,T}/C_{D,M}$ indicates for this example (fig. 11) that the element drag can contribute from about 20 to 35 percent of the total drag, the percentage depending on angle of attack and element shape. The variation of $C_{D,M}$ when spherical elements are present on the model is indicated in this figure for reference. An equally important result shown in figure 11 is indicated by the vertical bars at $\alpha = 0^\circ$. The variation in $C_{D,T}/C_{D,M}$ indicated by the magnitude of these bars for the two elements is the resultant deviation that can be expected in the element drag if the calculated value of δ is 20 percent less than the actual value. The drag coefficient calculated for the cylinder deviates only 3 percent, whereas the spherical drag coefficient calculation is in error by over 27 percent. This result provides an illustration of the attractiveness of those elements which exhibit a more nearly constant drag coefficient over a limited k/δ range.

Separation-Length Characteristics

An examination of the relationship between the separation length ahead of the tripping element (Δ) and the drag of these elements can be made by use of the oil-flow results. The variation of Δ/w with k/δ is shown in figure 12(a) for the spherical elements. A sketch has been provided in this figure to indicate how Δ was determined for both the two- and three-dimensional separation conditions. The separation length increases with k/δ as does $C_{D,t}$, although not as rapidly. (Compare with fig. 10.) The percent increase in Δ with a change in k/δ is strongly dependent on the spacing parameter; the largest percent increase of Δ with k/δ occurs at the highest s/w value.

To assess the effect of the spacing parameter s/w on the magnitude of Δ, figure 12(b) was constructed. Indicated on the curve for the 0.238-cm-diameter spherical element is the value of s/w (about $s/w = 7.8$) that divides the Δ/k curve into two- and three-dimensional separation. The separation lengths of all the element shapes and sizes vary similarly with s/w. A decrease in Δ/k with increasing s/w occurs as long as the separation is two-dimensional; predictably, when s/w has increased to a value such that an element is not influenced by its neighbors (three-dimensional separation), then further changes in element spacing do not measurably influence Δ. A

comparison of figures 12(b) and 9(b) indicates that an increase in s/w results in a decrease in both Δ and total drag. For a given element shape, the extent of separation ahead of the element is dependent on the same variables as the drag coefficient, that is, s/w and k/δ. The extent of separation is thus found to be indicative of the trend of the element drag coefficient when one of these variables is held constant.

Separation distances (normalized with respect to the total frontal area of the tripping elements) of all the element shapes tested herein are shown as open bars in the bar graph of figure 12(c). The separation parameter $\overline{\Delta}$ is referenced to the value of $\overline{\Delta}$ for the 0.238-cm-diameter spherical elements. If these separation-length results are compared with the corresponding normalized element drag values for these elements (filled bars in fig. 12(c)), it is found that no relationship appears to exist between $\overline{\Delta}$ and $C_{D,t}$ for different element shapes. The results of the comparison between separation length and drag for different element shapes thus indicate that the difference in the local flow characteristics around these elements preclude the existence of a simple relation between $\overline{\Delta}$ and $C_{D,t}$. If, however, only one element shape is of concern, then qualitative variation in $C_{D,t}$ can be predicted for a change in k/δ or s/w by comparison of separation distances.

CONCLUSIONS

Flow-field and drag characteristics of several tripping-element shapes have been examined under laminar-boundary-layer conditions at a free-stream Mach number of 6.8. The elements were located on both surfaces of two wedge-shaped models with rectangular planforms. The local Mach numbers of the models were 4.7 and 5.5. The results of the drag measurements and oil-flow patterns led to the following conclusions:

1. The element drag coefficient based on local conditions depends primarily on element shape, the spacing between the elements, and the ratio of the element height to the boundary-layer height. For the spherical elements, a correlation is developed in terms of the aforementioned variables.

2. In contrast to the spherical elements, the triangular prism and cylindrical elements advantageously exhibit drag coefficients which are relatively independent of the ratio of element height to boundary-layer height for values of this ratio that have practical application for hypersonic wind-tunnel facilities. Estimation of the drag contribution of these elements to model drag is greatly facilitated because of this independence.

3. For a given element shape, the extent of separation ahead of the element is dependent on the same variables as is the drag coefficient, that is, spacing between elements and the ratio of the element height to the boundary-layer height. The extent of separation

is shown to be a qualitative indication of the trend of the drag if either the spacing or the ratio of element height to boundary-layer height is held constant.

4. Multiple vortices produced in the separation region ahead of the protuberance pass around the element and are swept downstream.

Langley Research Center,
National Aeronautics and Space Administration,
Langley Station, Hampton, Va., July 28, 1969.

APPENDIX

CALCULATION OF ELEMENT DRAG FOR A WIND-TUNNEL CONFIGURATION

Aerodynamic coefficients on a delta-wing and half-cone-body combination without tripping elements present were reported in reference 15. The drag coefficients for a typical configuration without elements used in the present analysis were obtained from this reference. The values of $C_{D,M}$ shown in figure 11 are obtained by adding a calculated element drag value $C_{D,T}$ obtained from this study to the drag coefficient obtained from reference 15. The delta wing was swept to 70° and had a leading-edge bluntness of 0.064 cm. Tripping elements were assumed located on both upper and lower surfaces of the delta wing and at a chordwise distance of 1.25 cm from the leading edge. A 4w spacing was maintained in the spanwise direction, which resulted in a center-to-center spacing of about 11.7w.

To obtain $C_{D,T}$, the first step is to calculate the laminar-boundary-layer height at the element location from equation (32) of reference 7. Boundary-layer heights were calculated for both surfaces of the delta wing at the element location at several angles of attack. In this investigation, δ was calculated by assuming a purely chordwise (that is, flat plate) boundary-layer development from a sharp leading edge. This assumption is based on results from reference 16 which show that, in general, the laminar-boundary-layer growth proceeds independently of leading-edge bluntness and sweep. A roughness height of 0.15 cm was selected to provide a value of $k/\delta = 2$ at $\alpha = 0^{\circ}$. A new k/δ value was then computed for lower and upper surfaces from the local flow conditions at each angle of attack considered. The next step is to obtain $C_{D,t}$ for both upper and lower surfaces from figure 8 or 10 for respective k/δ values. Since this drag coefficient is based on the area of a circle of diameter equal to the element height and on the local dynamic pressure q_l, the coefficient must be adjusted to the conditions on which the drag coefficient of the model is based, that is, q_∞ and S. Thus at a given value of α, the value of the total element drag coefficient required for comparison with the measured values from the model in question is obtained from

$$C_{D,T} = C_{D,t} \times N \times \frac{A_c}{S} \times \frac{q_l}{q_\infty}$$

where N is determined by the spacing and the model chord length.

To evaluate q_l/q_∞ at the element location, the ratio can be rewritten as

$$\frac{q_l}{q_\infty} = \frac{p_l}{p_\infty} \times \left(\frac{M_l}{M_\infty}\right)^2$$

APPENDIX

The pressure and Mach number ratios were then estimated for the slightly blunted, swept-leading-edge model by the method of reference 16, with the result that $q_l/q_\infty = 0.985$ at $\alpha = 0^\circ$. Sweep and small leading-edge blunting effects on the q_l/q_∞ ratio largely compensate for one another. If an element spacing other than $s/w = 4$ is required in the application of the methods described herein, the drag coefficient change from the $s/w = 4$ spacing can be found from the results of figure 9.

REFERENCES

1. Braslow, Albert L.; Hicks, Raymond M.; and Harris, Roy V., Jr.: Use of Grit-Type Boundary-Layer-Transition Trips on Wind-Tunnel Models. NASA TN D-3579, 1966.
2. Holloway, Paul F.; and Sterrett, James R.: Effect of Controlled Surface Roughness on Boundary-Layer Transition and Heat Transfer at Mach Numbers of 4.8 and 6.0. NASA TN D-2054, 1964.
3. Sterrett, James R.; Morrisette, E. Leon; Whitehead, Allen H., Jr.; and Hicks, Raymond M.: Transition Fixing for Hypersonic Flow. NASA TN D-4129, 1967.
4. McLellan, Charles H.; Williams, Thomas W.; and Bertram, Mitchel H.: Investigation of a Two-Step Nozzle in the Langley 11-Inch Hypersonic Tunnel. NACA TN 2171, 1950.
5. Bertram, Mitchel H.: Exploratory Investigation of Boundary-Layer Transition on a Hollow Cylinder at a Mach Number of 6.9. NACA Rep. 1313, 1957. (Supersedes NACA TN 3546.)
6. Potter, J. Leith; and Whitfield, Jack D.: Effects of Slight Nose Bluntness and Roughness on Boundary-Layer Transition in Supersonic Flows. J. Fluid Mech., vol. 12, pt. 4, Apr. 1962, pp. 501-535.
7. Monaghan, R. J.: An Approximate Solution of the Compressible Laminar Boundary Layer on a Flat Plate. R & M. No. 2760, Brit. A.R.C., 1953.
8. Zubkov, A. I.; Panov, Ju. A.; and Voytenko, D. M.: Supersonic Gas Flow About the Cylinder on a Flat Plate. Fluid Dynamics Transactions, Vol. 3, W. Fiszdon, P. Kucharczyk, and W. J. Prosnak, eds., Państwowe Wydawnictwo Naukowe (Warsaw), 1967, pp. 627-638.
9. Morrisette, E. Leon; Stone, David R.; and Whitehead, Allen H., Jr.: Boundary-Layer Tripping With Emphasis on Hypersonic Flows. Viscous Drag Reduction, C. Sinclair Wells, ed., Plenum Press, c.1969, pp. 33-51.
10. Van Driest, E. R.; and McCauley, W. D.: The Effect of Controlled Three-Dimensional Roughness on Boundary-Layer Transition at Supersonic Speeds. Aerospace Sci., vol. 27, no. 4, Apr. 1960, pp. 261-271, 303.
11. Halprin, Robert W.: Step Induced Boundary-Layer Separation Phenomena. AIAA J. (Tech. Notes), vol. 3, no. 2, Feb. 1965, pp. 357-359.

12. Cary, Aubrey M., Jr.; and Morrisette, E. Leon: Effect of Two-Dimensional Multiple Sine-Wave Protrusions on the Pressure and Heat-Transfer Distributions for a Flat Plate at Mach 6. NASA TN D-4437, 1968.

13. Stainback, P. Calvin: Some Effects of Roughness and Variable Entropy on Transition at a Mach Number of 8. AIAA Paper No. 67-132, Jan. 1967.

14. Jones, Robert A.; and Hunt, James L.: Use of Fusible Temperature Indicators for Obtaining Quantitative Aerodynamic Heat-Transfer Data. NASA TR R-230, 1966.

15. Whitehead, Allen H., Jr.: Effect of Body Cross Section and Width-Height Ratio on Performance of Bodies and Delta-Wing—Body Combinations at Mach 6.9. NASA TN D-2886, 1966.

16. Creager, Marcus O.: The Effect of Leading-Edge Sweep and Surface Inclination on the Hypersonic Flow Field Over a Blunt Flat Plate. NASA MEMO 12-26-58A, 1959.

TABLE I.- SUMMARY OF GEOMETRIC AND FREE-STREAM VARIABLES

k, cm	R_∞, per m	k/δ	$R_{l,k}$	R_{l,x_k}
$\theta_m = 12.6^\circ$; $M_l = 4.7$				
0.198	0.30×10^7	2	0.89×10^4	2.77×10^5
	.68	3	2.03	6.31
	1.28	4	3.80	11.82
.238	.21	2	.76	1.95
	.46	3	1.65	4.24
	.84	4	3.05	7.81
$\theta_m = 7.7^\circ$; $M_l = 5.5$				
0.198	0.23×10^7	1	0.66×10^4	2.06×10^5
	.94	2	2.69	8.36
.238	.23	1.2	.80	2.06
	.35	1.5	1.20	3.07
	.63	2	2.19	5.62
	1.03	2.5	3.57	9.15
	1.48	3	5.12	13.10

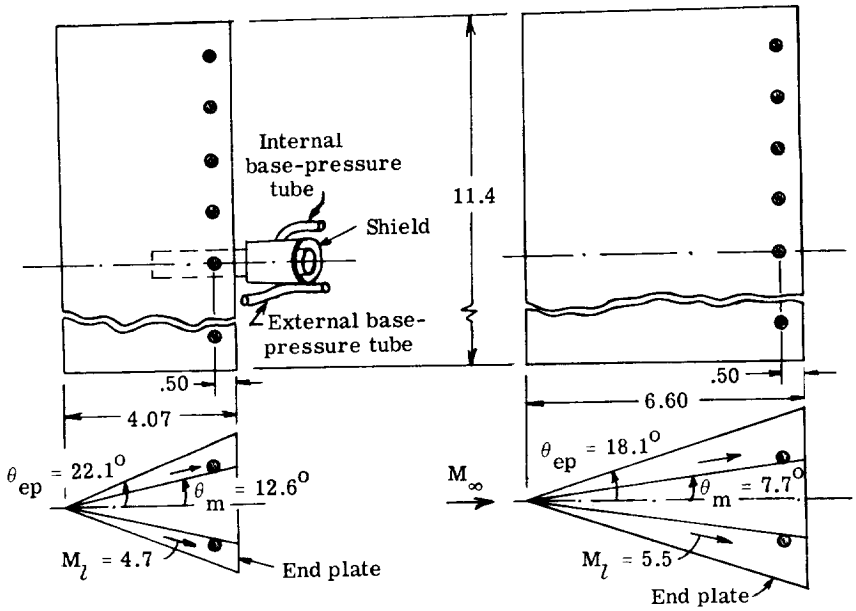

(a) Wedge models.

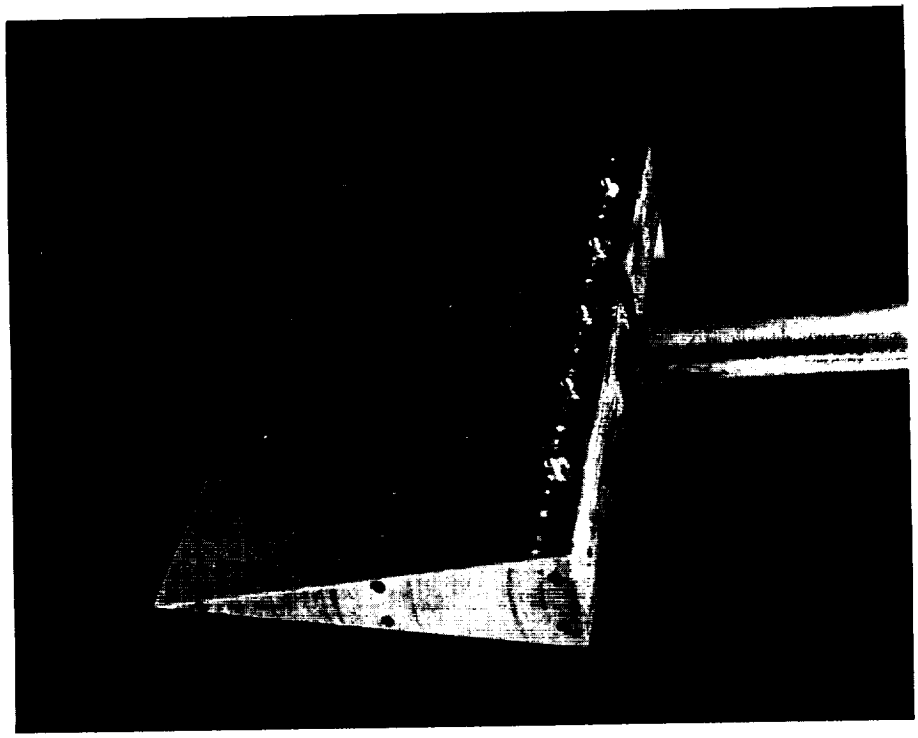

(b) Photograph of a model with one end plate removed and with 0.238-cm-diameter spheres as tripping elements. s/w = 8.

L-69-5267

Figure 1.- Models and tripping elements used in this investigation. All linear dimensions are in centimeters unless otherwise noted.

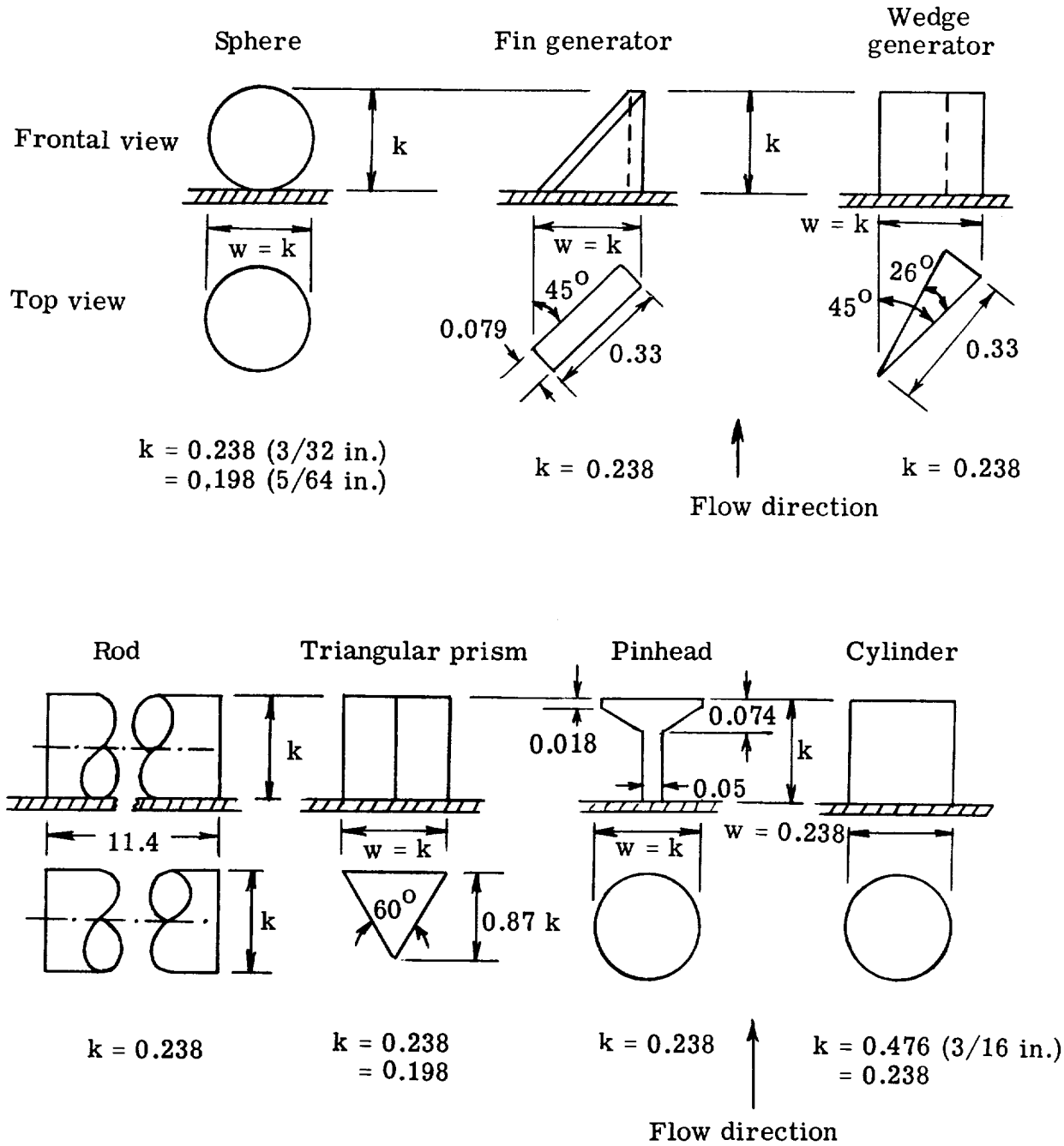

(c) Elements tested in investigation.

Figure 1.- Concluded.

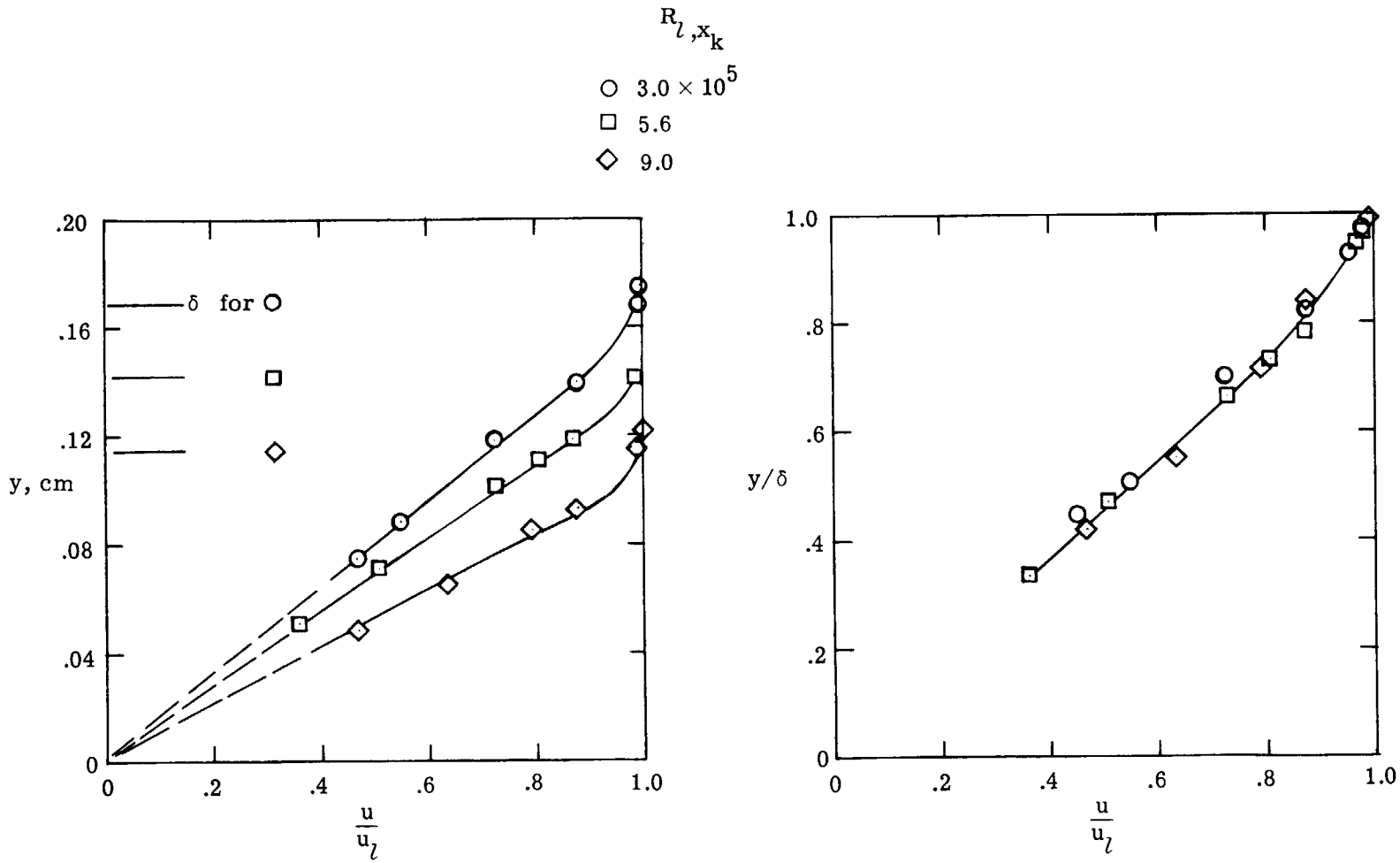

(a) Dimensional velocity profile.

(b) Similarity form.

Figure 2.- Velocity profiles at tripping-element location with elements absent. $\theta_m = 7.7^0$; $M_l = 5.5$; $y = \delta$ at $u/u_l = 1$.

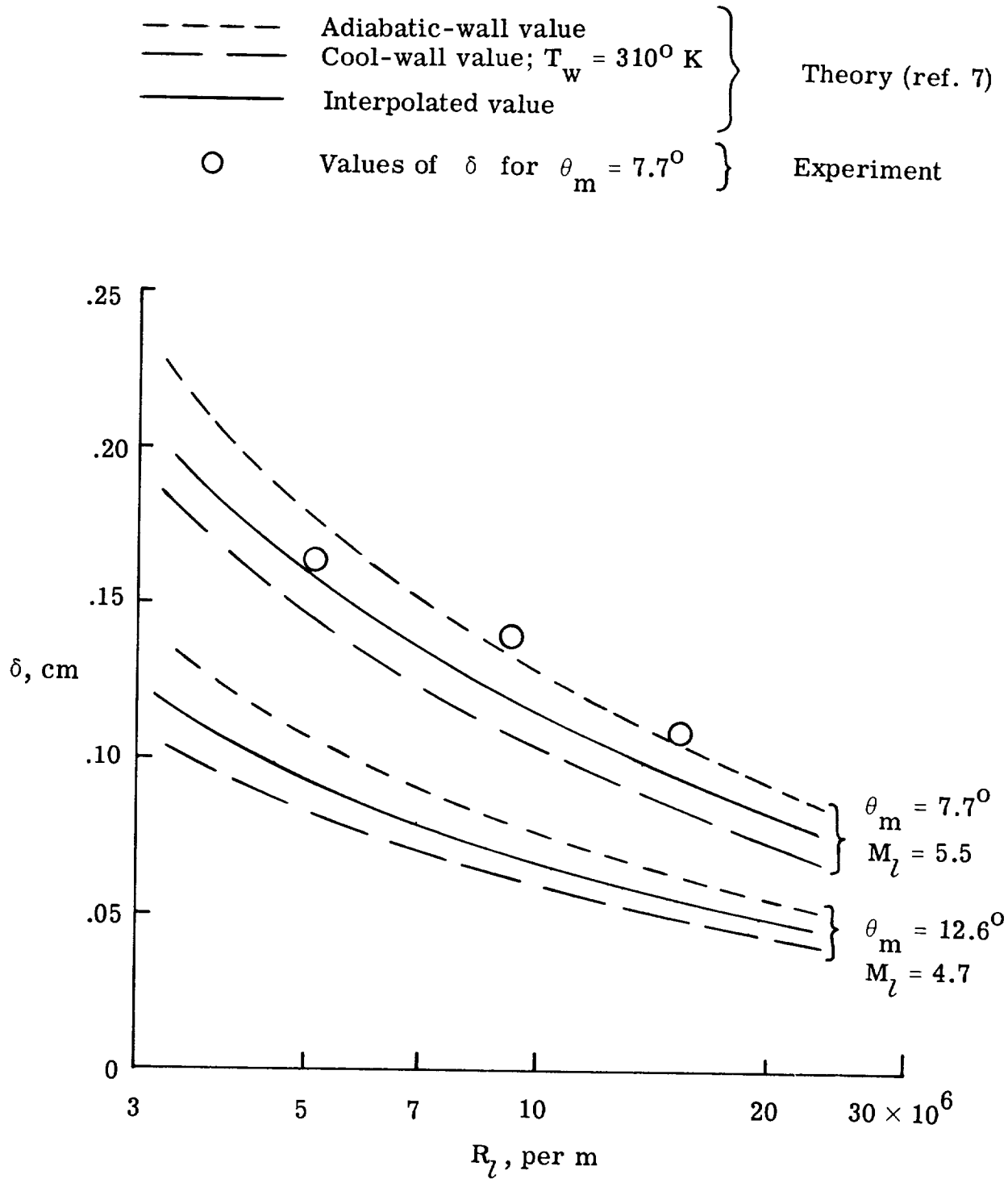

Figure 3.- Boundary-layer height at tripping-element location. $M_\infty = 6.8$; $y = \delta$ at $u/u_l = 1$ for theory and experiment.

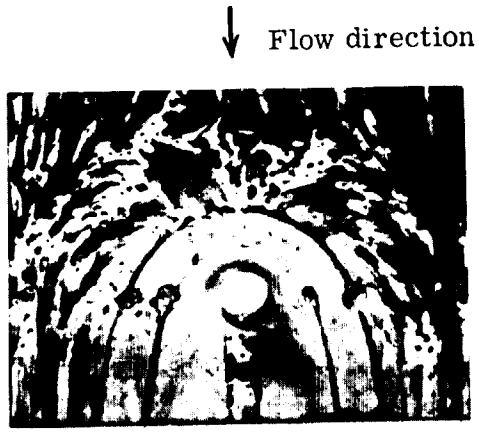

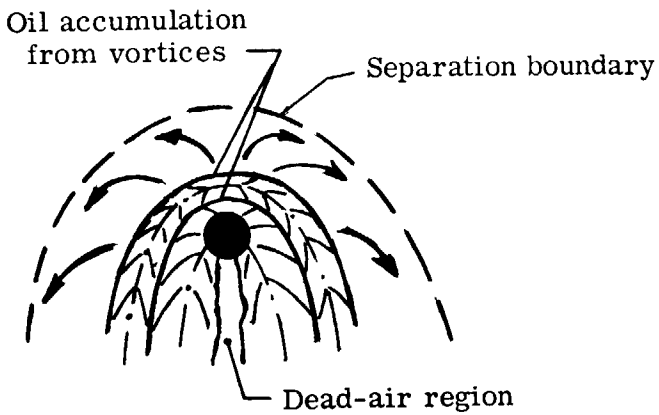

(a) Sphere.

(b) Cylinder.

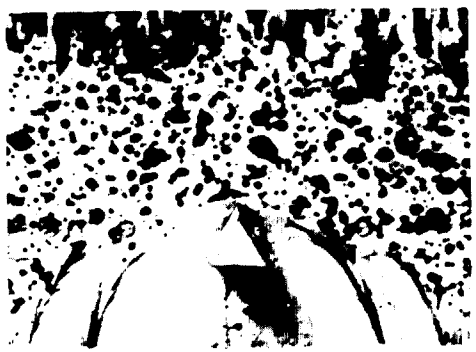

(c) Triangular prism.

(d) Pinhead.

Figure 4.- Flow behavior around elements. $M_l = 5.5$; $k/\delta = 2$; $s/w = 8$.

L-69-5268

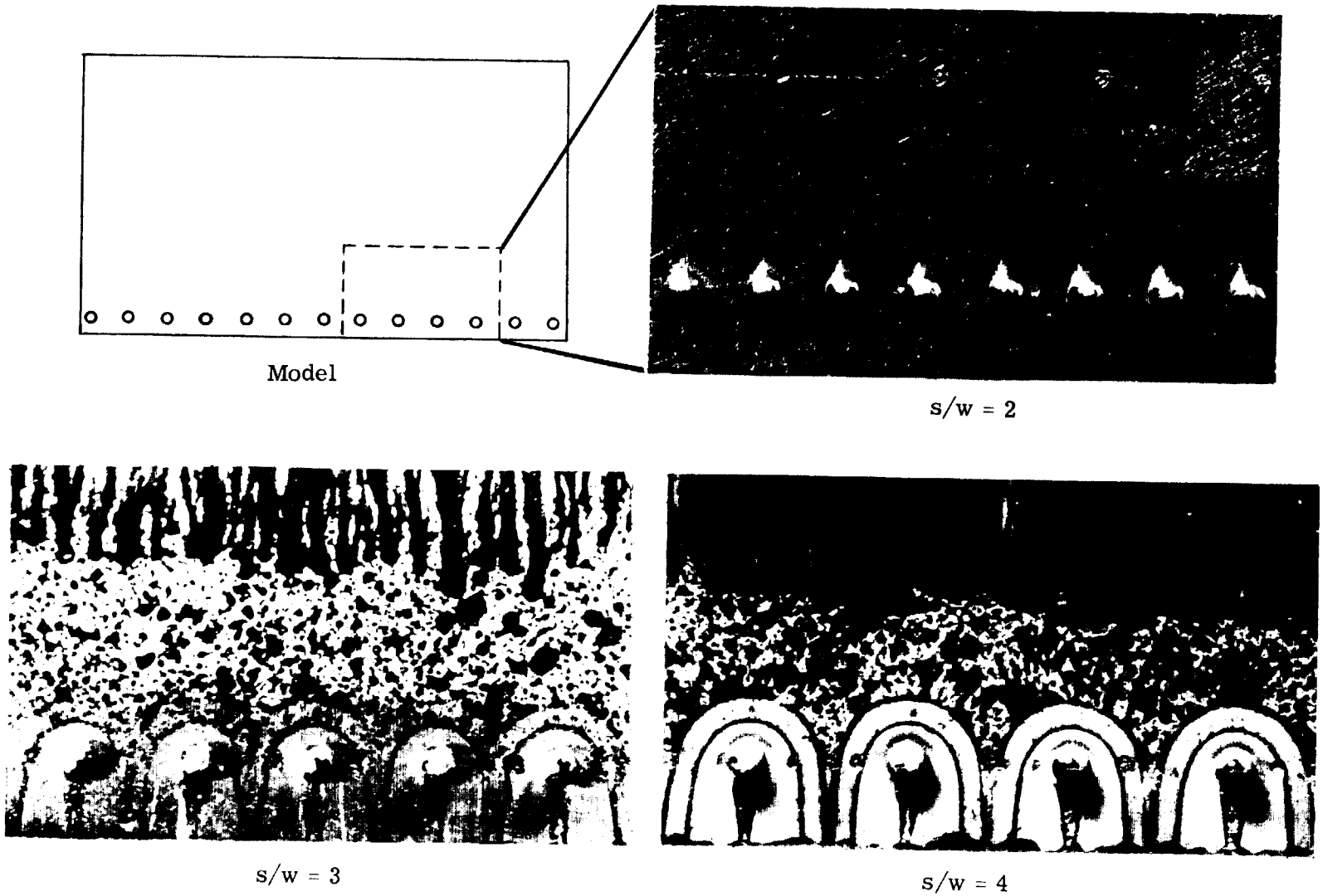

(a) Oil-flow patterns. s/w = 2, 3, and 4.

L-69-5269

Figure 5.- Effect of spacing on surface-flow patterns around spherical elements. $M_\ell = 5.5$; $k/\delta = 2$; $k = 0.238$ cm.

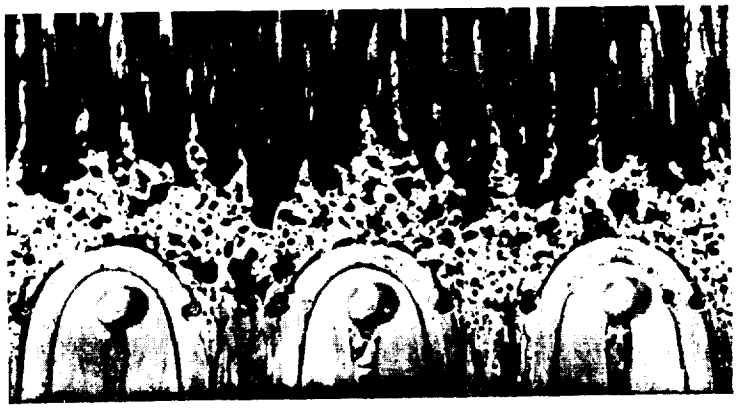

s/w = 6

s/w = 8

s/w = 16

(b) Oil-flow patterns. s/w = 6, 8, and 16. L-69-5270

Figure 5.- Continued.

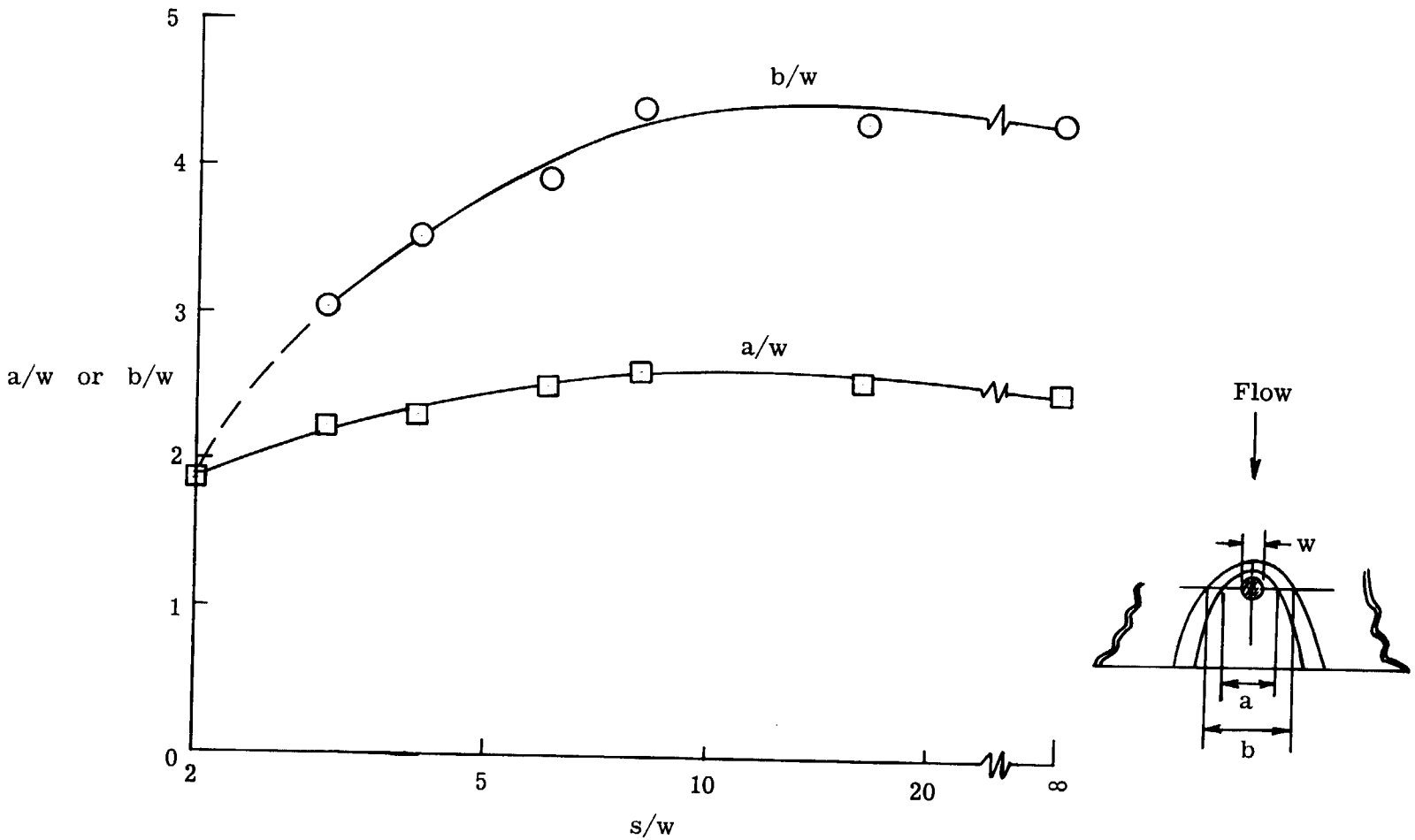

(c) Vortex-boundary measurements from oil-flow results.

Figure 5.- Concluded.

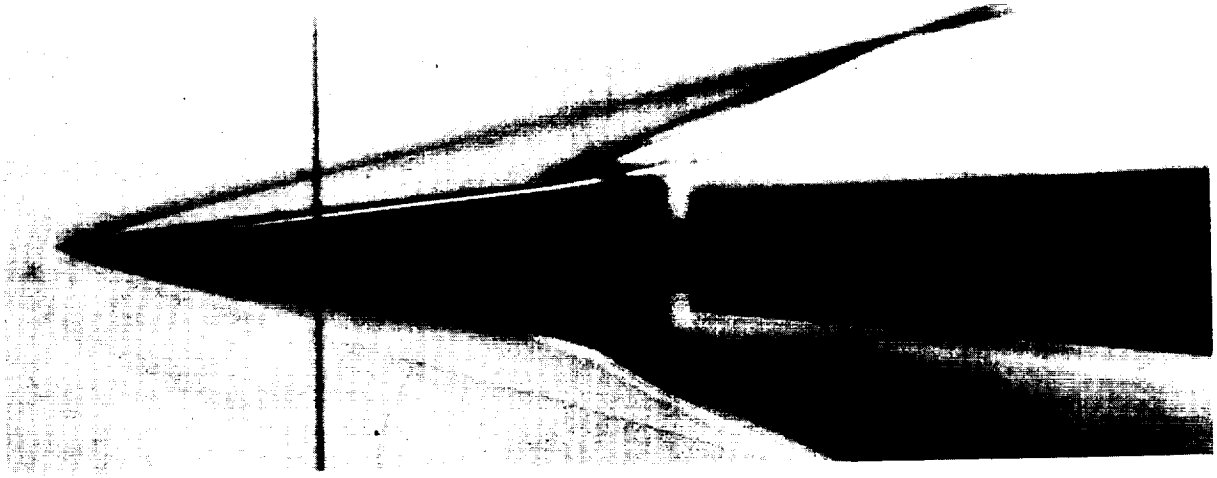

(a) Schlieren photograph.

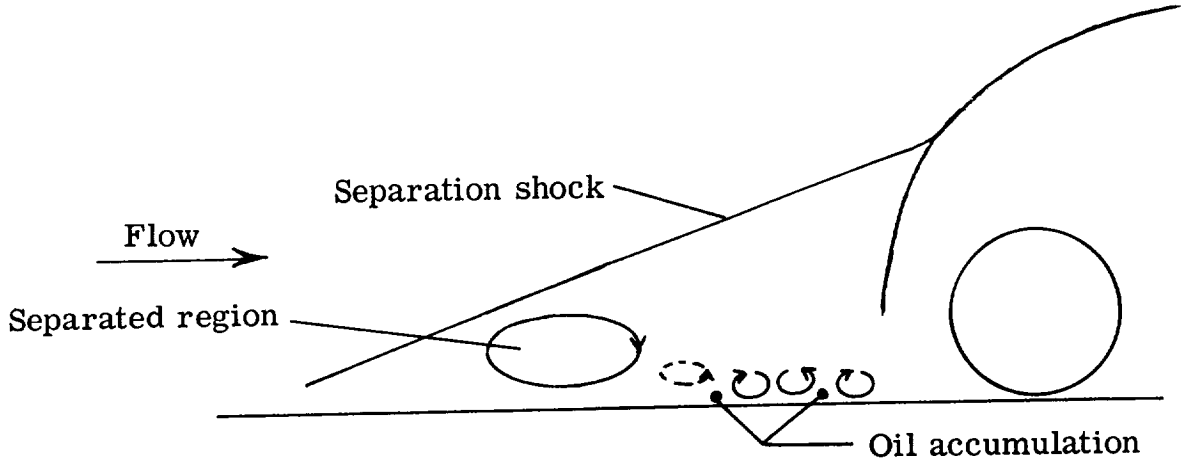

(b) Simplified flow-field schematic (chordwise cut at center line).

Figure 6.- Flow model for spherical element. $M_\ell = 5.5$; $k/\delta = 2$; $s/w \geqq 8$. L-69-5271

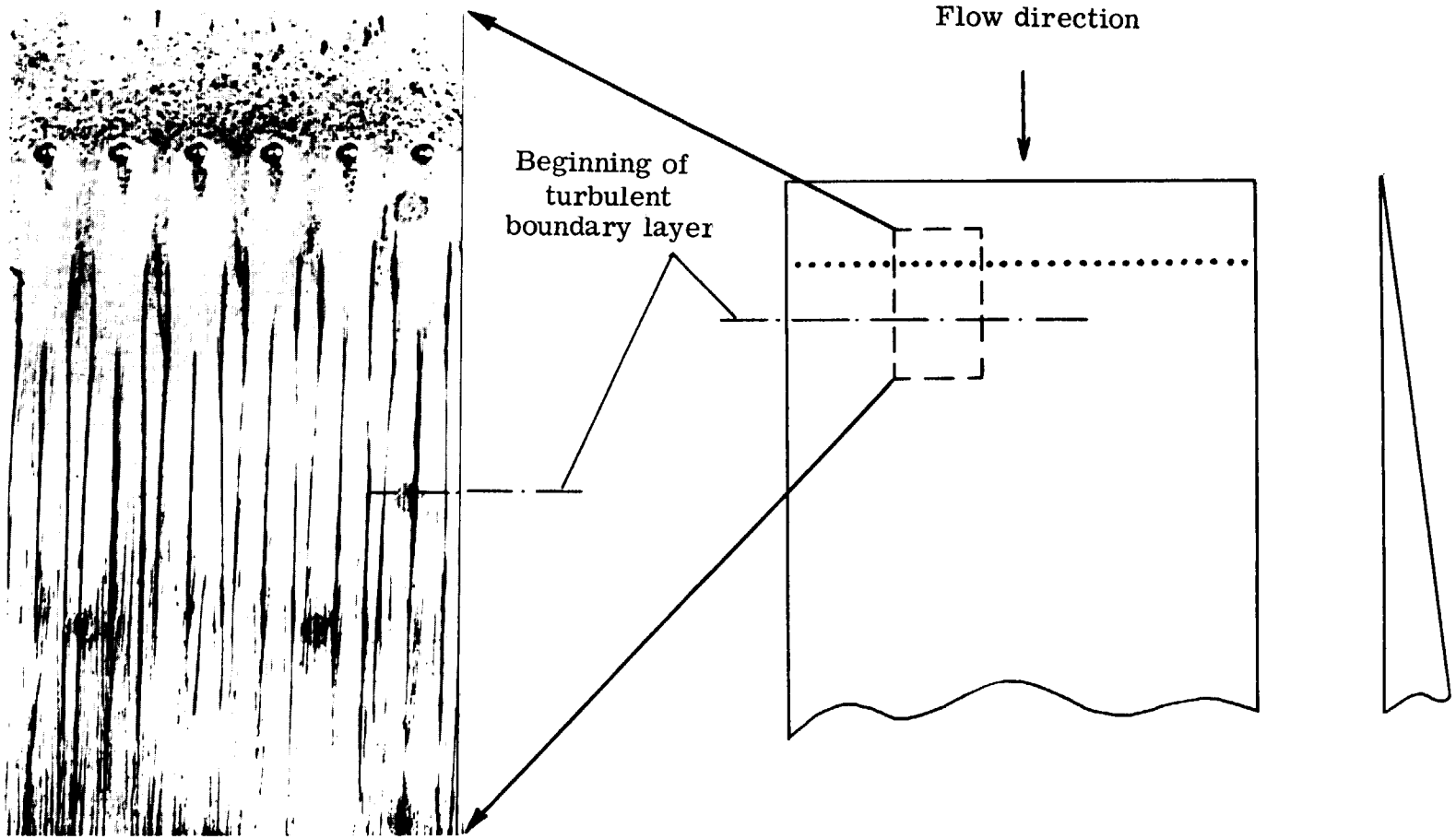

(a) Flat plate (ref. 12). $M_\infty = M_\ell = 6.0$; $k/\delta = 2$; $s/w = 4$.

L-69-5272

Figure 7.- Downstream influence of spherical elements.

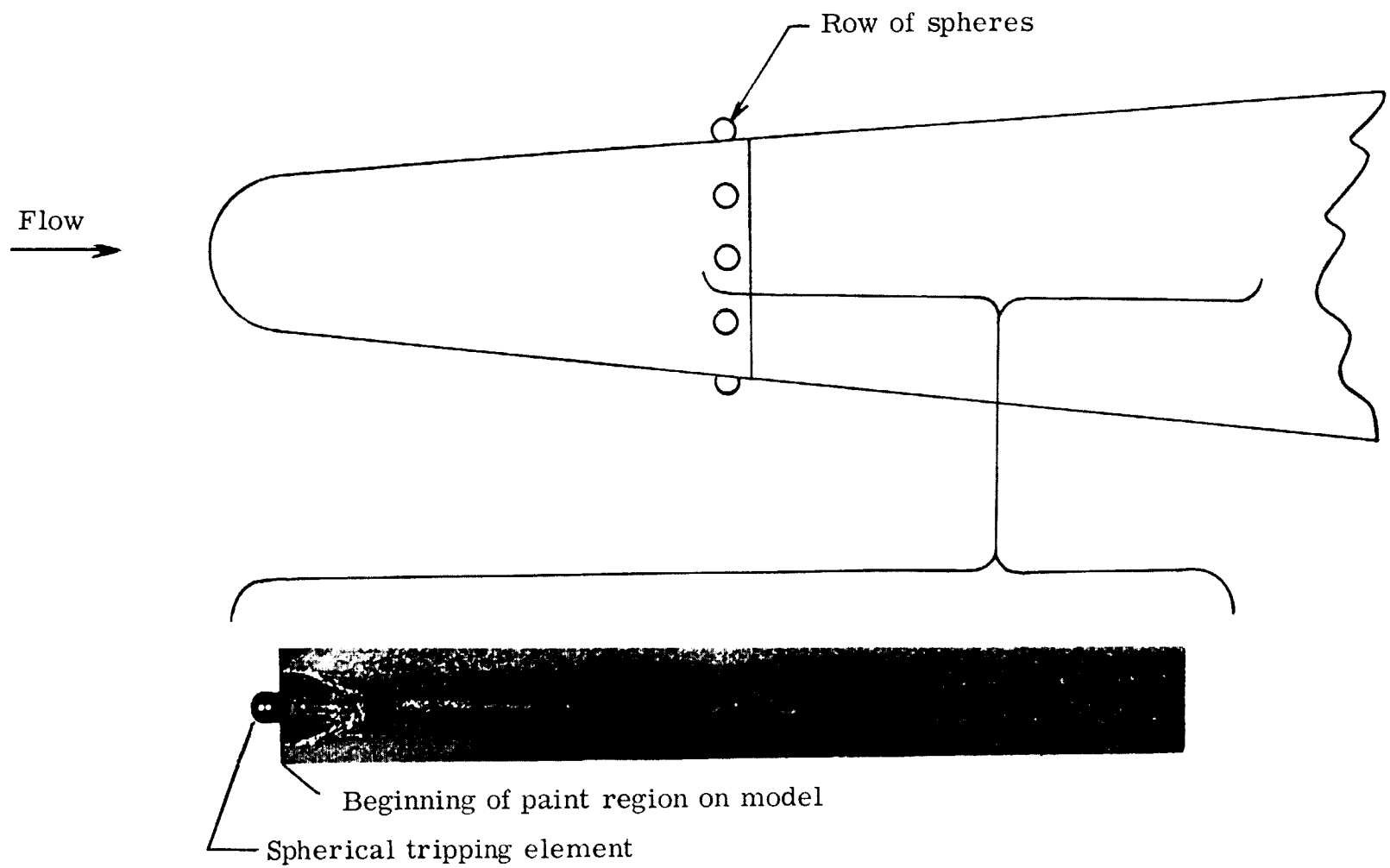

(b) 5° blunted cone (ref. 13). $M_{\infty} \approx 8$; $k/\delta = 2.4$; $s/w \approx 2.8$.

L-69-5273

Figure 7.- Concluded.

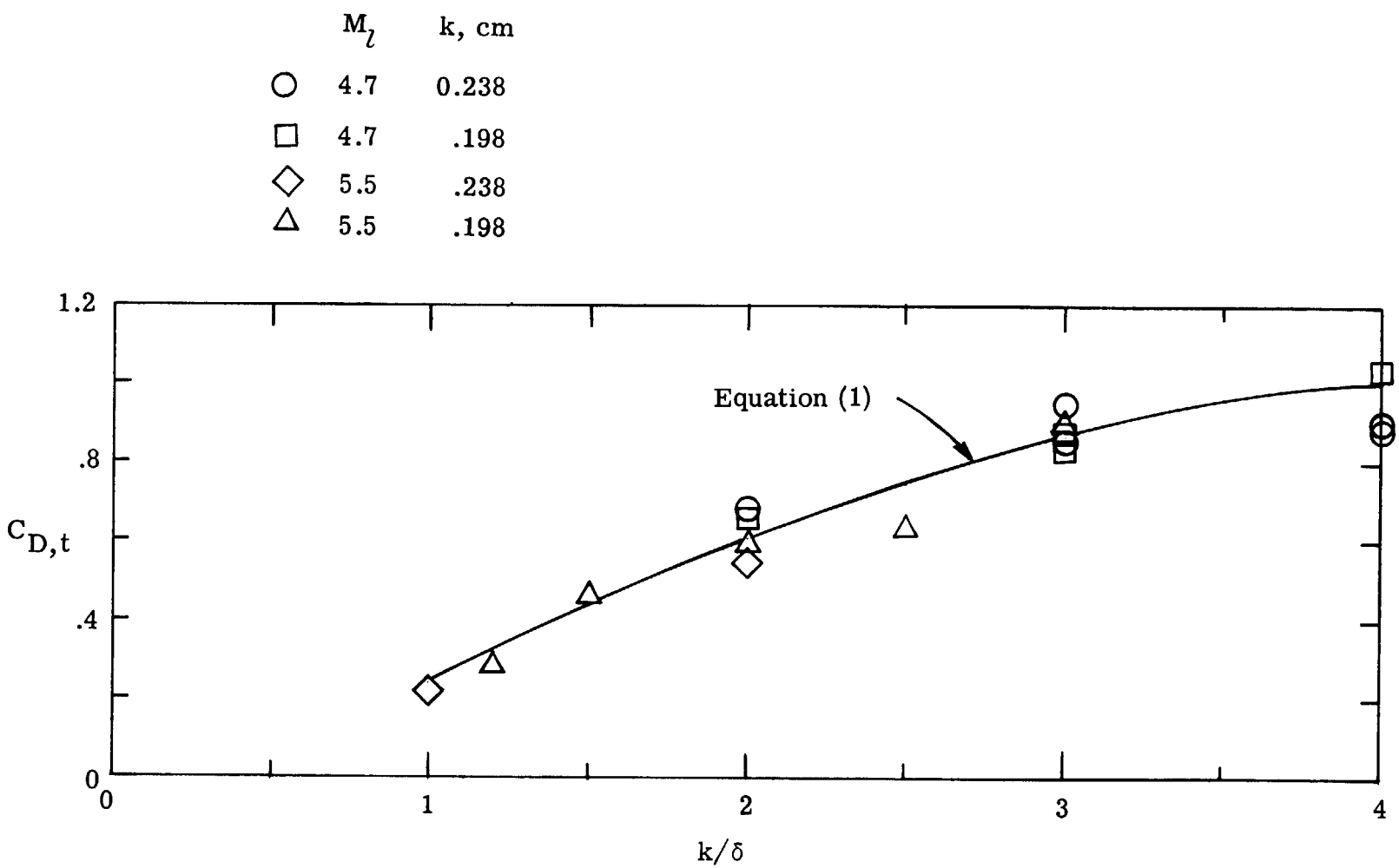

Figure 8.- Element drag correlation for spherical elements. s/w = 4.

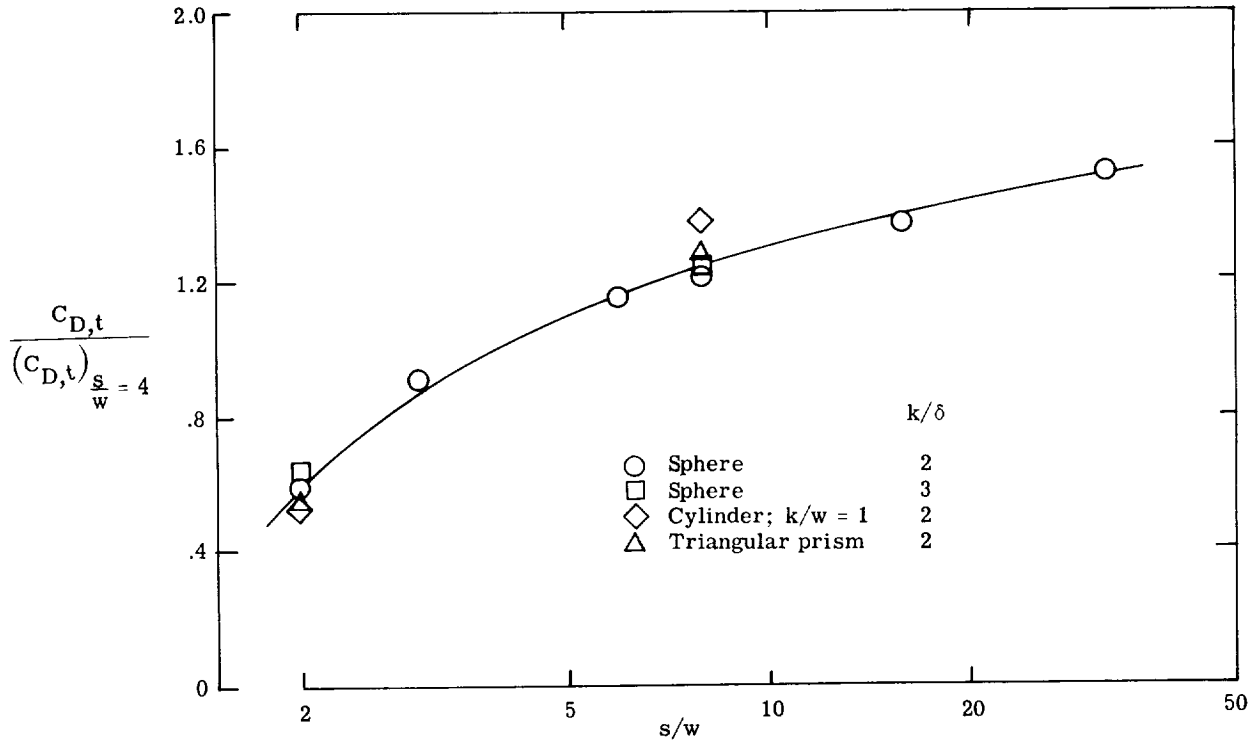

(a) Effect of element spacing on drag per element.

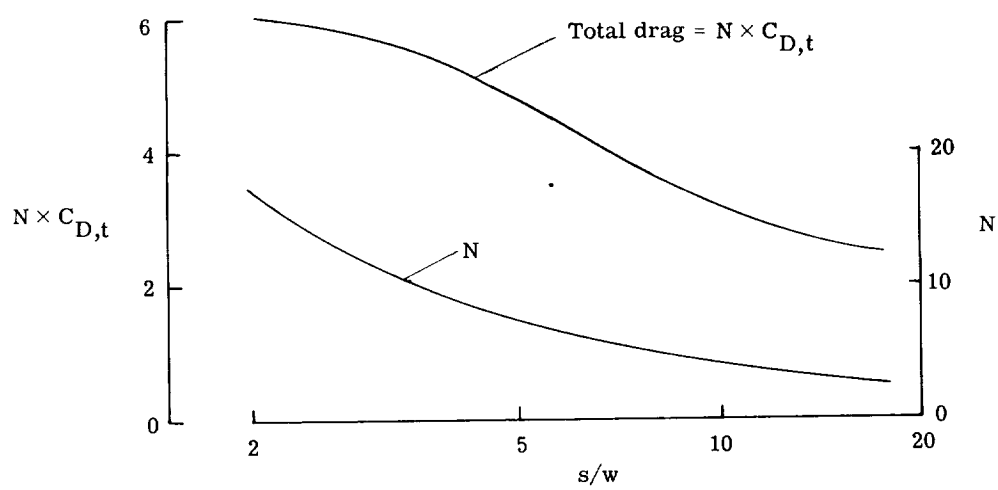

(b) Effect of element spacing on total drag of spheres; k/δ = 2; k = 0.238 cm.

Figure 9.- Element spacing effects on element drag. M_l = 5.5.

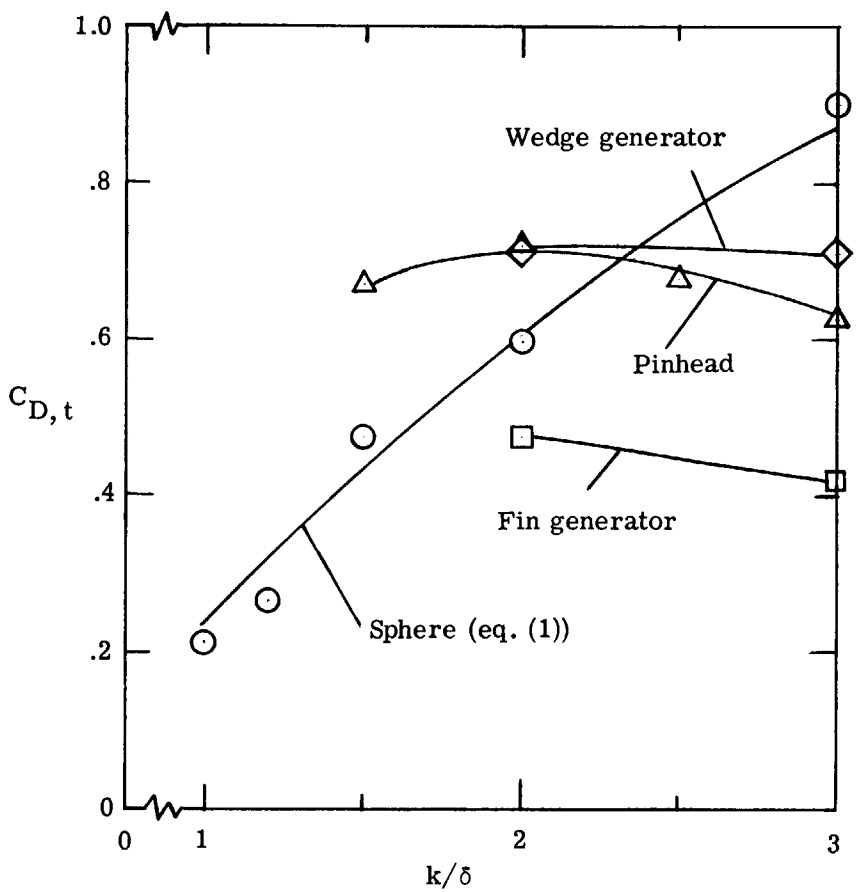

	Newtonian, $C_{D,t}$	A_c/A_F
○ Sphere	1.00	1.00
□ Fin generator	.58	1.56
◇ Wedge generator	1.11	.81
△ Pinhead	1.36	1.82

(a) Sphere, vortex generators, and pinhead. k = 0.238 cm.

Figure 10.- Comparison of element drag. M_l = 5.5; s/w = 4.

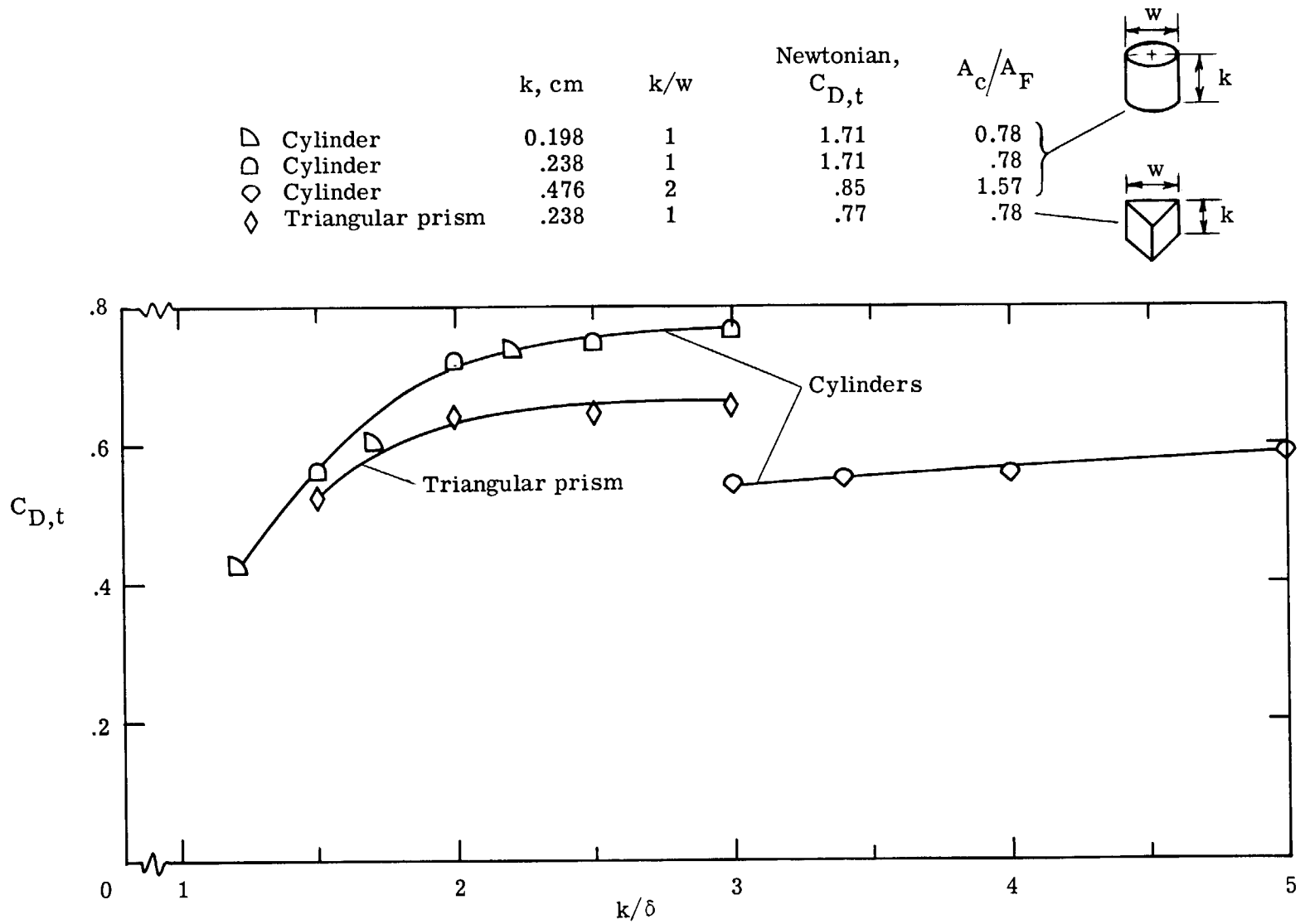

(b) Triangular prisms and right circular cylinders.

Figure 10.- Concluded.

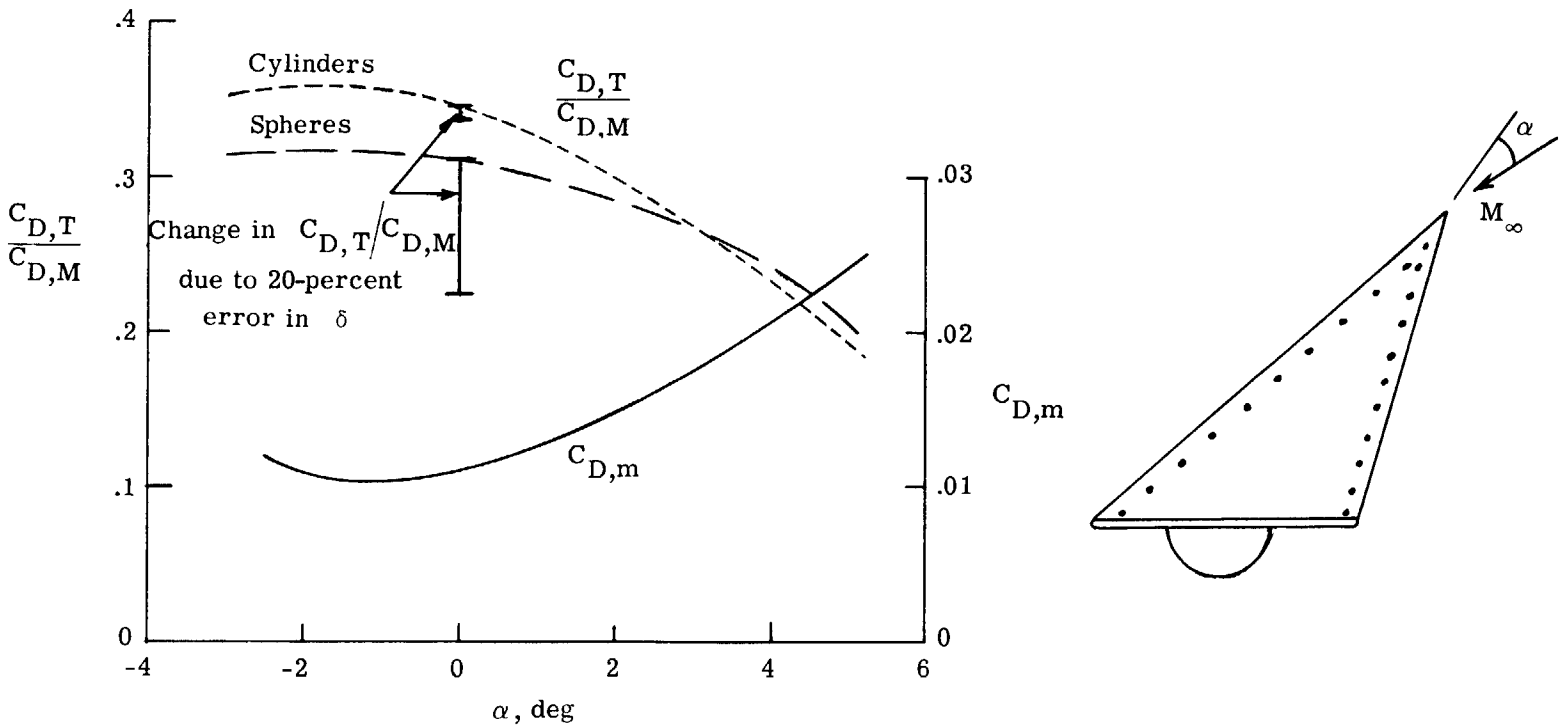

Figure 11.- Element-drag coefficients for typical wind-tunnel configuration. $M_\infty = 6.8$; $R_{\infty,L} = 1.4 \times 10^6$; $s/w = 4$; $k/\delta = 2$ at $\alpha = 0^\circ$; elements on both surfaces of wing.

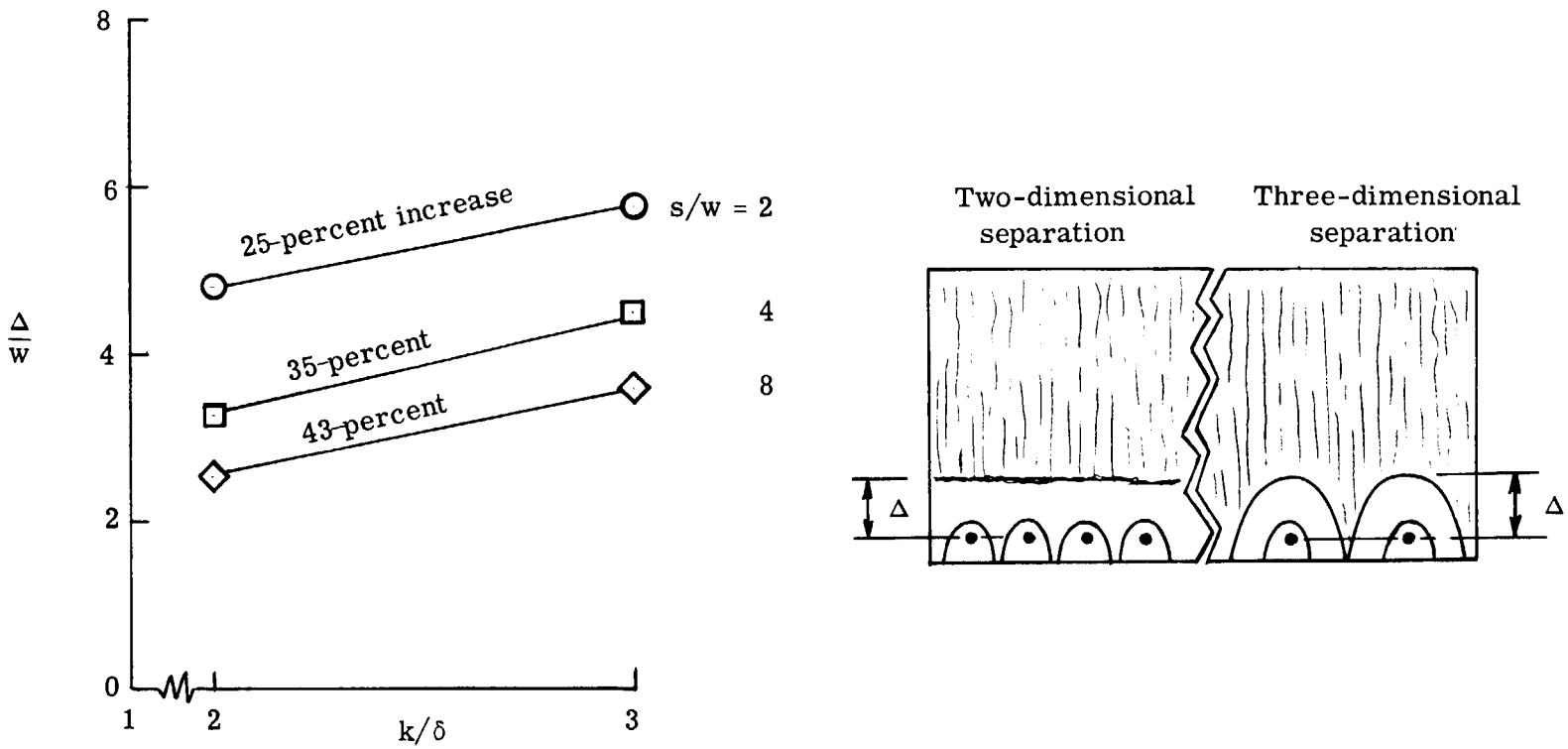

(a) Variation of Δ with k/δ for spherical elements; $k = w = 0.238$ cm.

Figure 12.- Examination of separation length Δ. $M_l = 5.5$.

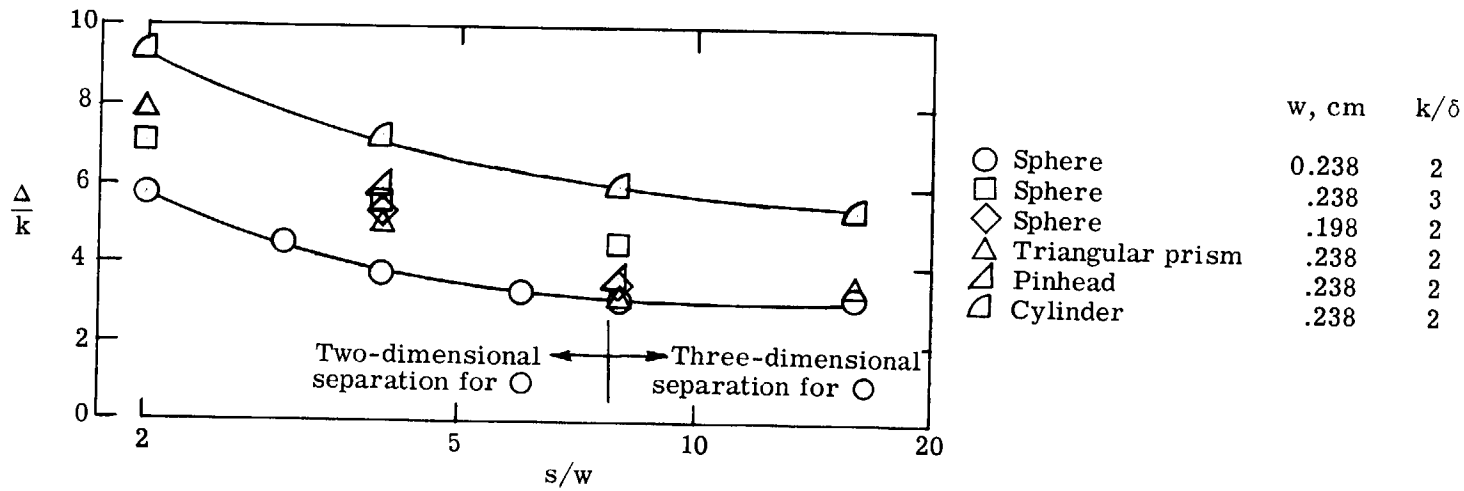

(b) Variation of separation length with spacing.

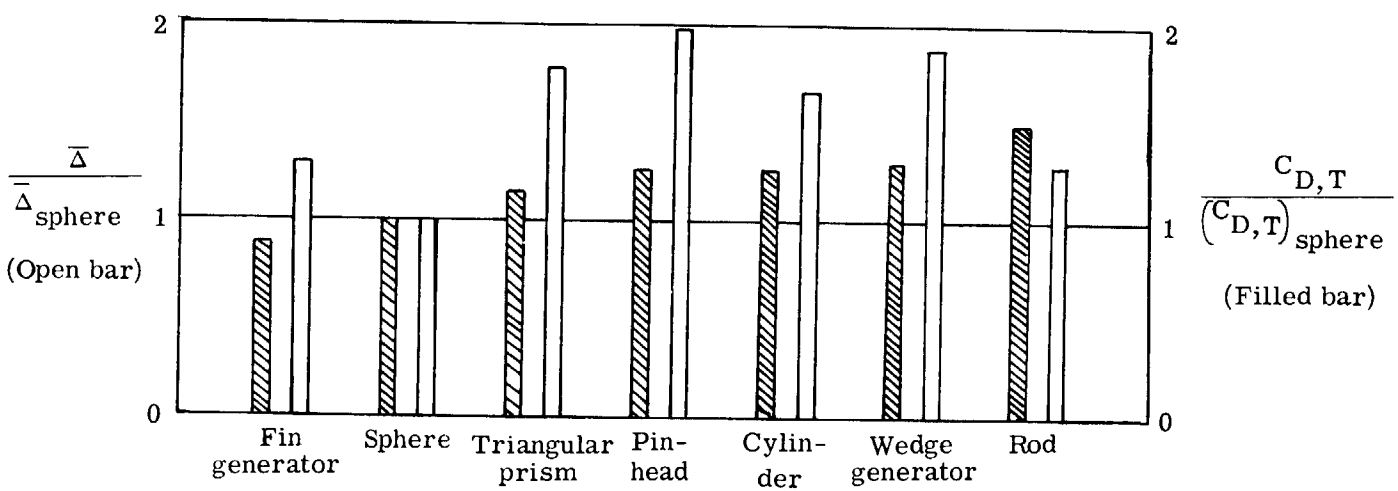

(c) Variation of $\bar{\Delta}$ and $C_{D,T}$ with element shape. $s/w = 4$; $k/\delta = 2$; $w = 0.238$.

Figure 12.- Concluded.